Journal of the Mechanics and Physics of Solids 59 (2011) 2323–2340

Contents lists available at SciVerse ScienceDirect

Journal of the Mechanics and Physics of Solids

journal homepage: www.elsevier.com/locate/jmps

Dynamics of inelastic deformation of porous rocks and formation of localized compaction zones studied by numerical modeling

Yu P. Stefanov [1], M.A. Chertov *, G.R. Aidagulov, A.V. Myasnikov

Schlumberger Moscow Research, Moscow, 119285, Pudovkina str. 13, Russia

A R T I C L E I N F O

Article history:
Received 16 July 2010
Received in revised form
2 August 2011
Accepted 8 August 2011
Available online 12 August 2011

Keywords:
Compaction localization
Constitutive behavior
Rock
Dynamics
Numerical algorithms

A B S T R A C T

The paper presents a numerical analysis of the inelastic deformation process in porous rocks during different stages of its development and under non-equiaxial loading. Although numerous experimental studies have already investigated many aspects of plasticity in porous rocks, numerical modeling gives valuable insight into the dynamics of the process, since experimental methods cannot extract detailed information about the specimen structure during the test and have strong limitations on the number of tests. The numerical simulations have reproduced all different modes of deformation observed in experimental studies: dilatant and compactive shear, compaction without shear, uniform deformation, and deformation with localization. However, the main emphasis is on analysis of the compaction mode of plastic deformation and compaction localization, which is characteristic for many porous rocks and can be observed in other porous materials as well. The study is largely inspired by applications in petroleum industry, i.e. surface subsidence and reservoir compaction caused by extraction of hydrocarbons and decrease of reservoir pressure. Special attention is given to the conditions, evolution, and characteristic patterns of compaction localization, which is often manifested in the form of compaction bands. Results of the study include stress–strain curves, spatial configurations and characteristics of localized zones, analysis of bifurcation of stress paths inside and outside localized zones and analysis of the influence of porous rocks properties on compaction behavior. Among other results are examples of the interplay between compaction and shear modes of deformation.

To model the evolution of plastic deformation in porous rocks, a new constitutive model is formulated and implemented, with the emphasis on selection of adequate functions defining evolution of yield surface with deformation. The set of control parameters of the model is kept as short as possible; the parameters are carefully selected to have simple and intuitive physical interpretation whenever possible. Results demonstrate that evolution of the yield surface with deformation has major influence on the resulting characteristics of deformation patterns, which is not sufficiently acknowledged in the literature.

1. Introduction

Studying the behavior of porous reservoir rocks under loading and developing mathematical description of the process is one of the topical problems of petroleum industry posed to rock mechanics and physics. Deformations in porous

* Corresponding author. Now at: Schlumberger Innovation Center, 1935 S. Fremont Drive, Salt Lake City, UT 84104, USA. Tel.: +1 801 974 2139; fax.: +1 801 584 2486.

E-mail addresses: Stefanov@ispms.tsc.ru (Y.P. Stefanov), MChertov@slb.com (M.A. Chertov), GAidagulov@slb.com (G.R. Aidagulov), AMyasnikov@slb.com (A.V. Myasnikov).

[1] Now at Institute of Strength Physics and Materials Science, Tomsk, 634021, pr. Akademicheskii 2/4, Russia.

0022-5096/$ - see front matter
doi:10.1016/j.jmps.2011.08.002

reservoirs, especially large irreversible ones, can have a large impact on an overall field profitably by, for example, changing the permeability of rocks, damaging or destroying wells, or causing subsidence and trap sealing failure. Developing efficient and accurate capabilities for modeling of compaction failure of reservoir rocks can also be useful for geoscientific applications outside the oilfield and for description of other porous materials, such as metal foams and bio-materials.

Failure of rocks in shear mode, including shear with dilatancy, which is typically observed under low to moderate values of mean stress is understood relatively better than the process of plastic deformation with its prevailing volumetric component of irreversible deformation or *compaction*, which takes place under higher levels of mean stress. Such levels of in-situ compressive stress are common for typical depths of hydrocarbon reservoirs, and well-known documented cases of land subsidence (Nagel, 2001) can only be attributed to substantial inelastic compaction of a pay zone. In the literature a number of laboratory experimental studies have documented important aspects of compaction of porous rocks (El Bied et al., 2002; Baud et al., 2006; Cuss et al., 2003; Fortin et al., 2005, 2006; Fossen et al., 2007; Karner et al., 2003; Olsson, 1999; Okubo and Schultz, 2005; Schubnel et al., 2005; Schultz and Siddharthan, 2005; Schutjens et al., 2004; Zhu and Wong, 1997).

Compaction can take place uniformly or with localization, depending on the conditions applied to the rock sample. At the same time, not many examples of field measurements are available to give a convincing picture of how the compaction is developed inside the porous reservoir because such measurements are costly. Usually, experiments both on the reservoir scale and in the laboratory can only record evolution of average parameters for the tested object, such as total deformation and total stress measured outside of the object, while detailed information about the distribution of deformation and stress field inside, and their evolution with time are unavailable. However, in the laboratory one can perform a detailed post-test microstructural analysis of the deformed structure.

This work focuses on a more detailed study of the compaction process itself using numerical simulation. This approach tracks the evolution of stress and strain distribution in time, as well as the development of the localization process and its connection with rock properties and loading conditions. It can also give new information about the interaction and switching between shear and compaction modes of deformation.

2. Theory

Before presenting the formulation of the numerical model for localized compaction and computer experiments on porous rock deformation, it is useful to overview main features of compaction revealed by experimental studies. Yield surfaces have been experimentally delineated for a number of porous rocks (Cuss et al., 2003; Schubnel et al., 2005; Schutjens et al., 2004; Tembe et al., 2008). Unlike low porosity rocks whose strength can be described by the Drucker–Prager or Mohr–Coulomb yield surfaces, porous rocks exhibit a decrease in strength with an increase in mean stress above a certain value, and the yield surface has a closed cap shape in the axes of stress intensity and mean stress.

Under high pressure, porous rocks can be deformed uniformly or non-uniformly with the formation of localized compaction bands as well as a localized shear compacting band. In loading experiments under high confining pressure, narrow compaction bands can form, with sub-perpendicular orientation to the highest compression axis. In low porosity rocks and in porous rocks under small mean pressures, cracks and bands of strain localization make an angle less than 45° to the maximum stress direction. In this case an intergranular fracture takes place, predominant inelastic deformation has shear mode and localized zones are often accompanied by dilatancy and loosening of rock. The slope of the localization band varies with pressure, porosity, and probably other factors. The shear strain component in the localization band depends on the slope provided that pure compaction occurs with a band orientation orthogonal to the axis of the highest compression (Rudnicki, 2004). In more detail, conditions of compaction and shear band formation are presented in the following papers: Garagash (2006), Issen and Challa (2003, 2006), and Issen and Rudnicki (2000).

When the level of confining pressure has intermediate values, too high to initiate pure shear localization and dilatancy, and too low to result in localized compaction with predominant porosity reduction and low shear, several zones of different types can be formed in the localization region. For instance, El Bied et al.'s (2002) study of Fontainebleau sandstone with 22% initial porosity demonstrated a case with a localization band composed of three sub-layers. In the internal central layer the rock was compacted and porosity was reduced to 10% by grain crushing. The two adjacent layers exhibited cracking of grains, loosening, and considerable increase of porosity up to 35%. Experimental studies indicate, that differences in porosity inside the compaction band and in the adjoining rocks can be as high as 20% (El Bied et al., 2002; Fortin et al., 2006; Fossen et al., 2007).

Experiments show that loading curves for compacting porous rocks subjected to triaxial loading can have rather different and complex forms with oscillations and stress reliefs (Baud et al., 2006; Cuss et al., 2003; Fortin et al., 2005, 2006; Zhu and Wong, 1997; Karner et al., 2003; Olsson, 1999; Klein et al., (2001)). Typical loading curves summarizing observations made in these papers and illustrating well-identified features of the compaction process are presented in Fig. 1. Fig. 1(a) illustrates the evolution of differential stress $Q=\sigma_1-\sigma_3$ (σ_1 and σ_3 are principal stresses) versus axial deformation of a specimen. Experimental evidence proposes that compaction band formation is manifested as a stress relief, sometimes with a tooth formation, and corresponding to the plateau in the diagram. After some amount of compaction and porosity reduction, further deformation occurs with stress increase. Fig. 1(b) represents a close-up of Fig. 1(a) near the yield point at different levels of confining pressure. Experimental observations show that with the

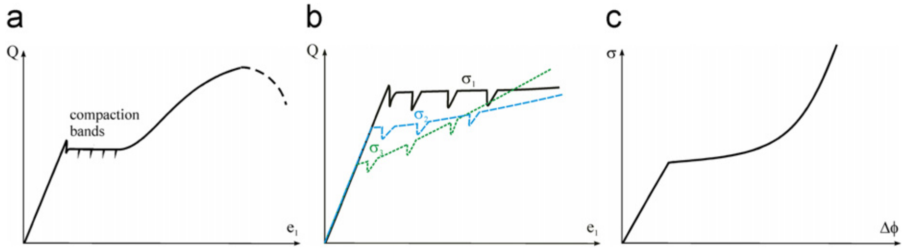

Fig. 1. Typical stress–strain curves in a triaxial experiment for porous rocks. Differential stress Q versus axial strain e_1 at different confining pressures (a, b) ($\sigma_1<\sigma_2<\sigma_3$) and mean pressure σ as function of porosity reduction $\Delta\varphi$ (c).

increase in confining pressure the effective strength is decreased and the slope angle of the loading curves is increased, having the typical shape of a hardening curve.

Fig. 1(c) presents a typical dependency of mean stress on volumetric strain or porosity changes. An interval having minimum slope can be identified on such curves right after the elastic limit, which is followed by the slope gradually increasing beyond the elastic one. Eventually the slope should reach a vertical asymptote, when all available pore space is exhausted. Gentle slopes correspond to the large rates of compaction, initiation of bands with localized compaction or bands with localized shear. Increasing slopes represent hardening of rock and decelerated reduction of porosity.

Taking into account the characteristic shape of the yield surfaces constructed on the basis of analysis and generalization of experimental observations, several cap models have been proposed for describing the behavior of porous rocks. Rudnicki (2004) and Grueschow and Rudnicki (2005) proposed to describe compaction with the use of an elliptical yield surface. Another big group of models is based on the combination of Mohr–Coulomb or Drucker–Prager yield surface in the zone of shear deformation and cap surfaces in the compaction zone. DiMaggio and Sandler (1971) and de Borst and Groen (2000) suggest an elliptical shape for the cap surface. The Carroll model implies a mobile parabolic surface, while Swan and Seo (1999) put forward the circular cap surface. All these variants of compaction yield surfaces suggest quadratic pressure dependence.

Unfortunately, these papers pay no proper and adequate attention to the *plastic potential*. This function is an essential part of the elastic–plastic simulations responsible for the post-failure description rock deformation. In particular, the majority of authors assume the application of an *associated flow rule*, that is, when the yield surface is used as a potential surface. This, however, reduces capabilities of the modeling, implying that the *dilatancy coefficient* is strictly related with the yield surface, which results in disagreement with experimental data. Undoubtedly, the use of a *non-associated flow rule* allows more accurate description of plastic deformation of rocks, but it requires the construction of an independent potential function with additional parameters, and related additional measurements. The accurate description of the evolution of the yield surface and its plastic potential surface is still a very complex question in studying and modeling the rocks' behavior. Many of these studies focus on the analysis of constitutive relations themselves; there are not so many examples of numerical modeling of plastic deformation of rock, which account for the localization in compaction.

As it was already noticed, physical processes in geologic materials can often take place *non-uniformly*. Mathematical models of material behavior are usually developed on the basis of experimental data describing the behavior of finite-size specimens; in doing so, the behavior of each point is assumed to correspond to the behavior of the entire specimen. However, the deformation of the specimen above the elastic limit is often localized; thus, the loading path can be different at each point. Stress and strain state can be inhomogeneous not only within the entire specimen, but also inside one compaction band or shear compacting band. Numerical simulations are, undoubtedly, a very convenient tool to evaluate the efficiency and adequacy of the constitutive equations for describing the behavior of not a single medium element, but a physical object as a whole, i.e., a specimen.

Most of the studies focus on the analysis of constitutive relations themselves without paying much attention to the modeling of inelastic deformation of a real object.

The purpose of this work is the analysis of the dynamics of deformation in porous rocks after failure resulting in strain localization during shear, dilatancy and compaction of the medium based on developed mathematical formulations required for performing the numerical calculations. Substantial attention is given to performing test calculations validating the algorithms and proper analysis of results for a better understanding of processes reproduced in such simulations. In this work, the deformation is modeled using dynamic analysis. The choice of the dynamic approach is dictated both by the physics of plastic deformation and fracture processes and by the possibility to trace the changes in properties during the deformation.

3. Mathematical models of porous rocks beyond the elastic limit

In low porosity rock, the formation of large damages is normally preceded by diffuse microcrack accumulation with an increase in volume (dilatancy) and strain localization. Damage accumulation, increased porosity and cracking can in turn change the sign of dilatation. In porous rock, the deformation can involve both dilation and compaction depending on the level of mean stress or rock pressure. The experimental data (El Bied et al., 2002) suggests that deformation can involve the formation of compacting bands as well as dilating bands during a single experiment. For any porous rock there are four pressure ranges with qualitatively different behavior, which can be distinguished as:

1. Low pressures, at which tensile stress may occur and operate towards failure. In this case, the possibility of the formation of tensile cracks should be taken into account. For this purpose, the appropriate fracture criteria and cracking algorithms must be used in the modeling.
2. Low to intermediate pressures. In this range, shear deformation is accompanied by dilation of rock; porosity increases. Increase in the mean stress results in the increase in shear strength. The behavior of rocks can be described in the framework of the Drucker–Prager–Nikolaevskii or Mohr–Coulomb models and a non-associated flow rule (Drucker and Prager, 1952; Nikolaevskii, 1971, 1972, 1996; Garagash and Nikolaevskii, 1989). The advantages of these methods are their validation by extensive experimental data, a range of applications, and presence in almost every applied software package.
3. High pressures. In this range, predominantly compaction takes place; rock grains or other microstructural elements of rock skeleton are crushed and porosity is reduced. Increasing the mean stress results in the decrease of shear strength. Here it is appropriate to rely on the elliptic-type yield surface. Rudnicki (2004) and Grueschow and Rudnicki (2005) give a very comprehensive review of compaction modeling using elliptic cap surface and the relation between the changes in different ellipse semiaxes and the volumetric and shear plastic strain components.
4. Intermediate pressures. In this range, the shear strength is close to its maximum and volumetric deformation is at minimum levels. The zero volumetric deformation of a rock sample can be achieved by either non-dilatant shear or by the combination of dilatant shear and equal and opposite compaction balancing the total change of volume. In the latter case, different peculiarities inherent to the pressure ranges 2 and 3, may reveal themselves. This may be connected with the inhomogeneity of the stress state and the inhomogeneity of the rock properties. The rock behavior can be described using a combination of yield surfaces.

Thus, for modeling of porous rocks in a wide loading range the *combined* yield surface acknowledging peculiarities of all pressure ranges is required. Moreover, experiments indicate that the yield surface and the plastic potential surface change during deformation. Therefore, in addition to the shape of the initial yield surface, there is a big concern about the type of dependencies describing the changes in the yield surface state and in the dilatation coefficient (the plastic potential surface state), including such dependencies as the function of mean stress. It becomes clear that description of the changes in limiting relations is more important than the choice of their initial form, because the amount of plastic deformation and the ratio between volumetric and shear components of deformation depends on it at every stage of plastic deformation process. This problem is likely to be the most challenging in the description of deformation of virtually all inelastic materials.

We used the combined model based on the truncated cone and elliptical yield surfaces. Here the conical part of the yield surface corresponds to shear failure zone and is a modification (from Stefanov, 2002, 2005) of the Drucker–Prager–Nikolaevskii's model with a non-associated flow rule. It is a well-known and recognized in the literature approach to describe shear deformation with dilatancy, supported by numerous experimental measurements of constitutive parameters for different rocks.

In the compaction failure zone, the elliptic yield surface is used. As in the model from Rudnicki (2004) and Grueschow and Rudnicki (2005), this approach assumes that the ellipse semiaxes depend on the shear and volumetric plastic strain components, respectively. Analysis of the most appropriate dependencies for *hardening* shows that good results can be obtained using a quadratic function for shear strains and a power law function for volumetric strains or changes in porosity. Current porosity can be a useful parameter for building up a unified hardening function for different rocks. Good results ensured by the quadratic dependency for shear strain hardening during simulations of low-porosity rocks (Stefanov, 2002, 2004, 2005) govern the use of a similar function for expansion of the yield surface. The model includes a non-associated flow rule with a variable dilatancy coefficient, which is dependent on the value of mean stress. This dependence, along with hardening, plays an important part in the formation of localization bands.

We constructed a combined surface (Fig. 2) consisting similarly to the DiMaggio–Sandler failure envelope of a Drucker–Prager cone in the shear (plastic dilation) zone:

$$f=\tau-\alpha\sigma-c=0 \tag{1}$$

and elliptical surface in the compaction zone:

$$f=(\sigma-p_0)^2/a^2+\tau^2/b^2-1=0, \tag{2}$$

where $\sigma=-\sigma_{kk}/3$ is the first stress invariant or mean pressure, $\tau=(s_{ij}s_{ij}/2)^{1/2}$ is the second deviatoric stress invariant or shear stress intensity, s_{ij} represents components of the stress tensor deviator, α and c are coefficients of internal friction and cohesion in the Drucker–Prager cone, $a=p_1-p_0$, b represents semiaxes of ellipse, p_0 is the threshold pressure between shear and compaction (center of ellipse), and σ_1 is the compaction onset pressure at zero shear or grain crushing pressure. In the tensile region, the yield surface is truncated by the corresponding tensile strength σ_t. However, we give no consideration here to tensile failure assuming that pressure is high enough. Concerning the four rock pressure ranges with

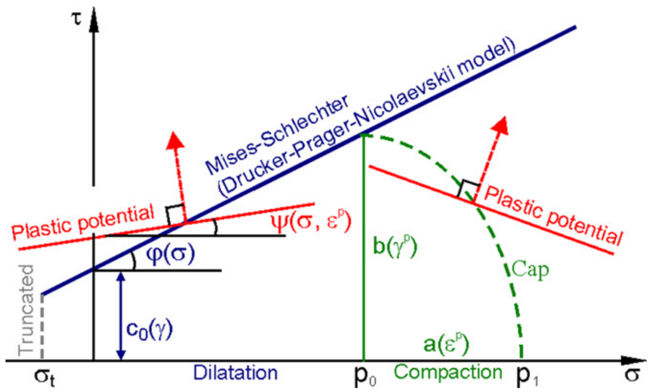

Fig. 2. Generalized combined yield surface for consolidated and porous media: σ_0 and σ_1 are mean pressure values, at which compaction of porous materials can be initiated under certain triaxial and hydrostatic compression (grain crushing pressure), respectively.

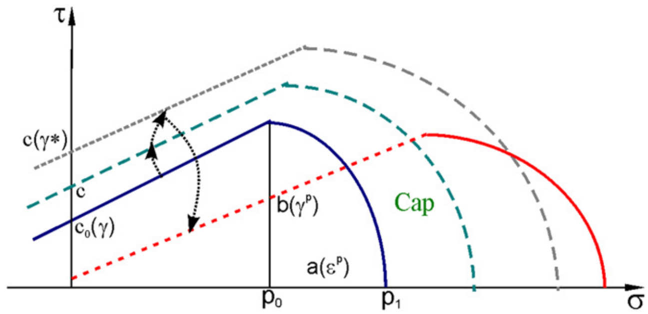

Fig. 3. Variation of the yield surface at different stages of the deformation process. In the plotted scenario hardening of material from either shear or compaction failure is followed by a decrease of cohesion and friction angle (softening).

different rock behavior described above, values near $\sigma=0$ correspond to low pressures, interval between 0 and p_0 – to low to intermediate ones, p_0 – intermediate and p_1 – high pressures.

Similarly to the DiMaggio–Sandler model, the upper point of the ellipse can slide along the cone surface during hardening. The minor semi-axis of ellipse b is defined through parameters of the center p_0, as well as through cone parameters α and c given by

$$b = c + \alpha p_0. \tag{3}$$

The way the grain crushing influences the yield surface is an important question. Different situations are possible during grain crushing and compaction depending on the grain material. At a certain stage of grain crushing, the number of contacts increases, which can result in a cohesion increase, so that the rock hardens. With further crushing, when ground grains of the medium fill the intergranular space and provide some lubrication, cohesion and friction decreases. During the entire compaction process the yield surface expands.

The yield surface variation during deformation (Fig. 3), takes place as materials harden and soften. The state of the cone surface is assumed to be determined by accumulated plastic shear strain γ^p:

$$c(\gamma^p) = c_0[1 + h(A(\gamma^p) - D(\gamma^p))], \tag{4}$$

$$A(\gamma^p) = 2(\gamma^p/\gamma^*) \tag{5}$$

$$D(\gamma^p) = (\gamma^p\gamma^*)^2, \tag{6}$$

where $A(\gamma^p)$ is the function of linear hardening and $D(\gamma^p)$ is the function describing damage accumulation during inelastic deformation and degradation of a rock connected to it. Shear strain intensity γ^p is calculated incrementally with $d\gamma^p = 2(((de_{ij})^p(de_{ij})^p)/2)^{1/2}$, $e^p_{ij} = \varepsilon^p_{ij} - (1/3)\varepsilon^p_{kk}\delta_{ij}$; h and γ^* are parameters controlling amplitude of cohesion variation (h) and level of accumulated plastic strain (γ^*), when degradation overcomes hardening and cohesion begins to decrease.

Elongation of the elliptical surface along the pressure axis (semiaxis a) and the center coordinate p_0, which determines compactions hardening, depend on accumulated volumetric strain. It is convenient to define the relation between variation of p_0 and a as functions of volumetric plastic deformation ε^p by

$$p_0(\varepsilon^p) = p_0^0\left(\frac{\varepsilon^*}{\varepsilon^* - \varepsilon^p}\right)^m, \tag{7}$$

and

$$a = a_0 + r\Delta p_0, \tag{8}$$

where ε^* is plastic volumetric deformation at ultimate compaction, m and r—parameters.

Assuming that the medium compacts only due to pore space reduction, (7) transforms to

$$p_0(\phi) = p_0^0(\phi^*/\phi)^m, \tag{9}$$

where $\varepsilon^* = \phi^*$, $\Delta\phi = -\varepsilon^p$, ϕ^* and ϕ are the initial and current porosity of the rock. Describing cap surface expansion and compaction hardening by the hyperbolic function (9), which assumes infinite cap expansion when $\phi \to 0$, is supported by the physical reason that as soon as porosity available for compaction is exhausted to zero the further plastic deformation can develop only in shear mode. This behavior reflects the existence of vertical tangent to stress–strain curve in Fig. 1(c).

It is convenient to use the plastic potential g in the form of the equation:

$$g = -\beta_1\sigma + \kappa\tau, \tag{10}$$

so that $\beta_1 = \sin\psi$, $\kappa = \cos\psi$, where angle ψ determines the slope of the plastic potential surface, and $(\beta_1/\kappa) = \beta$, where β is a classical dilatation coefficient defining the ratio between shear and volumetric strain increments. By definition of the dilatation coefficient, which has different sign for dilatation and compaction, angle ψ has to be different in shear and compaction regions of the yield surface. Mathematically, the direction of the plastic strain vector can be parameterized by the confining pressure. The variation of the dilatancy coefficient in the proposed model is defined in terms of a stress-dependent multiplier, which is a power law function of volumetric stress:

$$\beta_1(\sigma) = \beta_0\left(\frac{p_0 - \sigma}{p_0}\right)^{n_1} \quad at \;\; \sigma < p_0,$$
$$\beta_1(\sigma) = -\left(\frac{\sigma - p_0}{p_1 - p_0}\right)^{n_2} \quad at \;\; p_0 < \sigma < p_1. \tag{11}$$

Eq. (11) defines gradual rotation of the vector of plastic potential gradient starting with maximum dilatancy β_0 at low confining pressures, passing the moderate levels of confinement, when at the top of the yield surface at $\sigma = p_0$ dilatancy is zero, going to "negative dilatancy" or compaction on the cap and ending with maximum compaction on the pressure line, which corresponds to purely hydrostatic compression.

Summarizing the list of parameters of the proposed inelastic model, for description of plastic deformation in shear region ($\sigma \le p_0$) we need the following parameters:

c_0, α—parameters of initial yield surface (cohesion and friction angle);
h, γ^*—hardening parameters;
n_1, β_0—parameters of the plastic potential (dilatancy parameters).

In compaction region ($p_0 < \sigma \le p_1$):

p_0, p_1—parameters of cap surface (initial);
$\varepsilon^* \approx \phi^*$, r, m—parameters of cap expansion (hardening);
n_2—parameter of plastic potential for compaction.

Since the main emphasis in this work is made on the inelastic behavior of porous rocks during compaction, some of the parameters controlling the slope of the failure surface and dilatancy parameters in the shear interval are fixed in all conducted simulations: $\alpha = 0.5$, $\beta_0 = 0.3$, $n_1 = 2$. Other parameters are varied as needed to investigate dynamics of compaction process and compaction localization.

4. System of governing equations

Deformation processes in geological media are simulated using an approach based on solving the system of dynamic equations for an elastic–plastic medium by an explicit numerical scheme (Wilkins, 1964, 1999).

The system of equations used to describe deformation processes includes:

$$\text{equation of continuity}: \quad \rho V = \rho_0 V_0, \tag{12}$$

$$\text{equations of motion}: \quad \sigma_{ij,j} + \rho F_i = \rho \dot{u}_i\,. \tag{13}$$

Here ρ_0, V_0 and ρ, V are the initial and current density and volume of representative elements of a material; u_i are velocity vector components, σ_{ij} are the Cauchy stress tensor components, F_i are mass forces, where the dot above a variable denotes the Lagrange time derivative, and the subscript after a comma represents the corresponding coordinate derivative.

Here and below the standard convention for the summation over repeated indices is assumed. As internal energy changes are not taken into account in the constitutive equations of these models, the energy conservation equation is excluded from the system.

For the strain rate tensor$\dot{\varepsilon}_{ij}$ it is assumed that

$$\dot{\varepsilon}_{ij} = \dot{\varepsilon}^{\mathrm{e}}_{ij} + \dot{\varepsilon}^{\mathrm{p}}_{ij}, \tag{14}$$

where $\dot{\varepsilon}^{\mathrm{e}}_{ij}$ and $\dot{\varepsilon}^{\mathrm{p}}_{ij}$ are the elastic and plastic parts of strain rate, respectively.

The relation between stresses and strains for the elastic behavior are described by the hypoelastic law:

$$\sigma_{ij} = -\sigma\delta_{ij} + s_{ij}, \tag{15}$$

$$\frac{Ds_{ij}}{Dt} = 2\mu\left(\dot{\varepsilon}^{e}_{ij} - \frac{1}{3}\dot{\varepsilon}^{e}_{kk}\delta_{ij}\right),$$
$$\frac{Ds_{ij}}{Dt} = \dot{s}_{ij} - s_{ik}\dot{\omega}_{jk} - s_{jk}\dot{\omega}_{ik}, \tag{16}$$

$$\dot{\sigma} = -K\frac{\dot{V}}{V}. \tag{17}$$

The stress tensor is decomposed into a spherical σ and deviatoric parts s_{ij}. The components of the strain rate tensor $\dot{\varepsilon}_{ij}$ are calculated by differentiation of velocities:

$$\dot{\varepsilon}_{ij} = \frac{1}{2}(u_{i,j} + u_{j,i}), \tag{18}$$

and $\dot{\omega}_{ij}$ are the rotational velocity tensor components:

$$\dot{\omega}_{ij} = \frac{1}{2}(u_{i,j} - u_{j,i}), \tag{19}$$

δ_{ij} is the Kronecker delta symbol, K and μ are the bulk and shear moduli, respectively.

Calculation of the plastic strain is defined by the yield surface and plastic potential equations:

$$f(\sigma_{ij}, \varepsilon^{p}_{ij}) = 0, \tag{20}$$

$$g(\sigma_{ij}, \varepsilon^{p}_{ij}) = 0, \tag{21}$$

$$d\varepsilon^{p}_{ij} = \lambda\frac{\partial g}{\partial\sigma_{ij}}, \tag{22}$$

where f is the yield surface function, g is the plastic potential, λ is a non-negative multiplier defined during deformation and $\varepsilon^{\mathrm{p}}_{ij}$ represents the plastic (inelastic) strain components.

Deformation $\varepsilon^{\mathrm{p}}_{ij}$ above the elastic limit is calculated using a procedure based on the instantaneous adjustment of stresses to the yield surface (Stefanov, 2002, 2005; Stefanov and Thiercelin, 2007). Note, that stresses may be alternatively adjusted with consideration for relaxation time. It is assumed, that at each subsequent time step plastic strain increments are proportional to the difference between stresses calculated from the elastic law and stresses corresponding to the yield surface. The first calculation step, after the grid point coordinates are determined and total strain increments are calculated, is to preliminarily calculate stresses from the elastic law, denoting these stresses by an asterisk, and denoting by an index n stresses from the previous time, which are not outside the yield surface:

$$(s^{n+1}_{ij})^* = s^{n}_{ij} + (\Delta s^{n+1}_{ij})^*,$$
$$(\sigma^{n+1})^* = \sigma^{n} + (\Delta\sigma^{n+1})^*. \tag{23}$$

After that, the transition to the plastic state has to be checked by substituting preliminary stress values $(\sigma^{n+1}_{ij})^*$ into the yield surface equations (1–2). If $f^* = f(\sigma^*_{ij}) \le 0$, the state of material in a given computational grid cell is inside the yield surface, (it is in the elastic state), the preliminary calculated stress state is a true one and we can move to the next time step taking $\sigma^{n+1}_{ij} = (\sigma^{n+1}_{ij})^*$.

In the case when $f^* = f(\sigma^*_{ij}) > 0$, the point in the stress space is outside the yield surface, and the plasticity condition is satisfied: the element of the simulated medium has transformed into the plastic state and some part of its strain is inelastic. The plastic strain component has to be calculated and it has to correspond to relaxation of stresses from preliminary, non-physical, $(\sigma^{n+1}_{ij})^*$ values to some stresses, which are among the possible stress states of the medium inside the yield surface, $f(\sigma^{n+1}_{ij}) \le 0$.

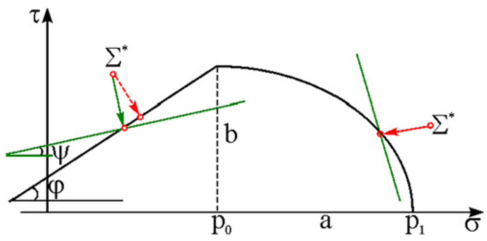

Fig. 4. Scheme of correcting the stress to the yield surface.

The use of an associated flow rule would mean that from this preliminarily calculated stress state in the point Σ^* (Fig. 4) the stress state would be moved perpendicularly towards the yield surface (dotted arrow in Fig. 4). In the case of a non-associated flow rule, when the equations for yield surface and plastic potential do not coincide, the point in the stress space moves perpendicularly towards the plastic potential surface until it intersects with the yield surface (Fig. 4). The yield surface and plastic potential surface of a medium may change during deformation, which is described in the proposed non-associative model using (4)–(6), (8), (9) and (11); however, it is assumed that inside a single numerical time step, which is sufficiently small, the yield surface is unchanged and plastic potential is described by a linear function (10) with constant coefficients.

For calculation of plastic strain increments expression (22) can be written in a slightly different form (Grueschow and Rudnicki, 2005; Rudnicki, 2004):

$$d\varepsilon_{ij}^{p} = d\lambda\left(\frac{s_{ij}}{\tau}G_\tau - \frac{1}{3}G_\sigma\delta_{ij}\right), \tag{24}$$

where $\sigma = -(\sigma_{kk}/3)$ is the first stress invariant, $\tau = (s_{ij}s_{ij}/2)^{1/2}$ is the second deviator stress invariant, and

$$G_\tau = \partial g/\partial\tau,$$
$$G_\sigma = \partial g/\partial\sigma. \tag{25}$$

The plastic shear strain intensity $d\gamma^p = 2(((de_{ij})^p(de_{ij})^p)/2)^{1/2}$ can be written as

$$d\gamma^p = G_\tau d\lambda, \tag{26}$$

where $e_{ij}^p = \varepsilon_{ij}^p - (1/3)\varepsilon_{kk}^p\delta_{ij}$.

The bulk part of plastic strain $d\varepsilon^p = -(d\varepsilon_{kk})^p$ is defined by

$$d\varepsilon^p = G_\sigma d\lambda \tag{27}$$

Then, the expressions for plastic strain acquire the form:

$$d\varepsilon^{pl} = \lambda\frac{\partial g}{\partial\sigma} = -\lambda\beta_1, \tag{28}$$

$$d\gamma^p = \lambda\frac{\partial g}{\partial\tau} = \lambda\kappa, \tag{29}$$

$$\tau = \tau^* - \lambda\kappa\mu, \tag{30}$$

$$\sigma = \sigma^* + \lambda\beta_1 K. \tag{31}$$

Here, the asterisk denotes the stress state parameters corresponding to Σ^*. The value of λ can be calculated from the distance needed to move in the stress space from the unrelaxed value of the yield function f^* in Σ^* to the yield surface, while the direction of movement is specified by the plastic potential.

For the Drucker–Prager part of the yield surface $f = \tau - \alpha\sigma - c$ one can find

$$\lambda = f^*/(\kappa\mu + \alpha K\beta_1). \tag{32}$$

For the elliptical part of the yield surface $f = ((\sigma - p_0)^2/a^2) + (\tau^2/b^2) - 1$, the parameter λ can be found from

$$A\lambda^2 + B\lambda + C = 0, \tag{33}$$

where

$$A = (\kappa\mu)^2 + (R\beta_1 K)^2; \quad B = 2(R(\sigma^* - p_0)\beta_1 K - \tau^*\kappa\mu);$$
$$C = f^* = f(\sigma^*) = R(\sigma^* - p_0)^2 + \tau^{*2} - b^2; \tag{34}$$

$$R = (b/a)^2.$$

$$\lambda_{1,2} = \frac{-B \pm \sqrt{B^2 - 4AC}}{2A}, \tag{35}$$

The smallest positive root from (35) has to be selected in order to find the intersection point of the normal to the plastic potential surface and the ellipse segment in the region $\tau > 0$, $\sigma > p_0$. Substituting it into (28–31), one can find values of stress invariants belonging to the yield surface and corresponding strains at a certain point of the medium at the current moment of time. After the stress invariants are calculated, the components of stress are determined as:

$$s_{ij} = s^*_{ij} \frac{\tau}{\tau^*} \tag{36}$$

similarly to the procedure described in Wilkins (1964, 1999) and Stefanov (2002, 2005).

5. Computational results and discussion

To focus on the study of general features of compaction process dynamics and compaction localization, we carried out numerical simulations of compressive loading of porous specimens using a simple and easy-to-interpret problem statement (Fig. 5). All modeled specimens have a rectangular shape and are composed of homogeneous porous rock. Dimensions of samples were 30×60 mm, which is a 1:2 ratio of edges, grid sizes were 50×100 or 100×200. Numerical simulation is performed in 2D plane strain, when

$$u_z = 0, \quad \dot{u}_z = 0, \quad \dot{\varepsilon}_{xz} = \dot{\varepsilon}_{yz} = \dot{\varepsilon}_{zz} = 0. \tag{37}$$

The specimens were subjected to non-hydrostatic compression, when vertical and horizontal stresses are unequal, in two stages. During the first stage of loading, vertical and horizontal stresses were increased simultaneously until the horizontal stress reached a prescribed value of lateral confinement σ^c, which was then kept at fixed level. During the second stage the top side of the specimen was subjected to a given displacement rate, which resulted in increasing axial stress, denoted σ^1, which was also the maximum principal stress and all aspects of the deformation process were recorded.

The driving force for rock compaction in petroleum reservoir is the reduction of pore pressure, which for roughly constant overburden weight results in the proportional increase of effective stress in the rock matrix. For a single dry sample applying external hydrostatic loading is equivalent to uniform reduction of pore pressure in a saturated specimen. To scale the simulation results to a petroleum reservoir it is necessary to bear in mind that the stress path in depleted reservoir is better approximated by proportional variation of vertical and horizontal loading, while a fixed lateral confining pressure is more convenient for the implementation in the laboratory and interpretation of the results.

During the numerical simulation it was ensured that the mean stress was sufficiently high and the stress path in specimens passed from elastic to inelastic state through the cap region. Configuration of the problem and loading sequence was the same in all numerical tests considered in this work; the level of confinement and rock properties controlled by the parameters in constitutive equations were varied to analyze the compaction process under different conditions.

For testing purposes, modeling started with simulation of the deformation of specimens under hydrostatic compression in the XY plane. Fig. 6(a) depicts curves for the variation of total volume, plastic volumetric deformation, and shear plastic deformation in the case of 10% initial porosity of the sample. Rock properties (except porosity) are taken from Table 1. The largest variation of volumetric strain and porosity reduction happened during a relatively limited increase of pressure, after the stresses reached the cap surface. Fig. 6(b) represents the variation of hydrostatic pressure as a function of total volumetric strain in the cases of 10% initial porosity (1) and 30% initial porosity (2). The slope of the pressure/volumetric strain curve is shown to change during compaction similarly to the experimental evidence (Baud et al., 2006; Cuss et al., 2003; Karner et al., 2003).

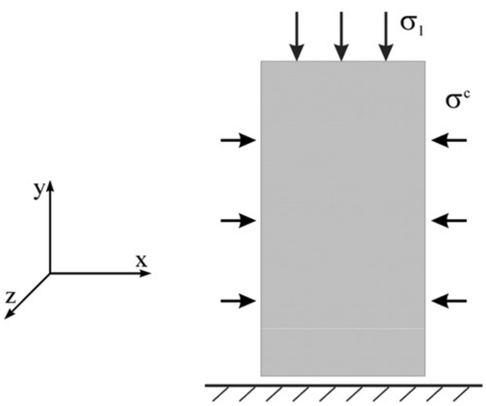

Fig. 5. Scheme of specimen loading.

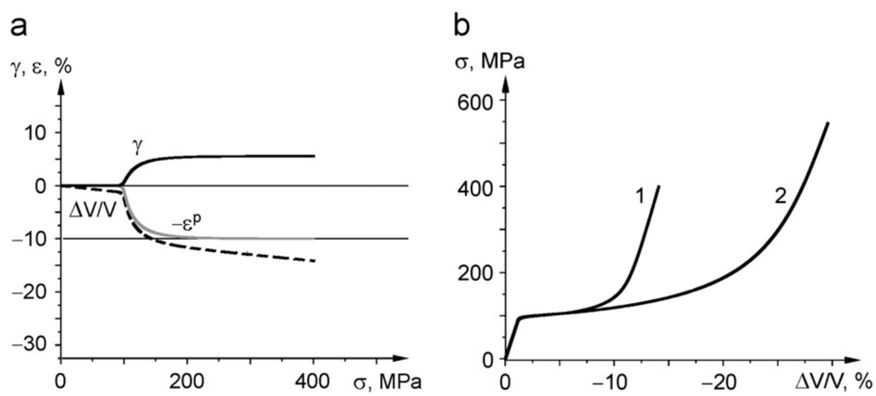

Fig. 6. Volumetric and shear strain versus mean pressure (a) and mean pressure versus volumetric strain (b) in uniform compression of a porous sandstone specimen.

Table 1
Parameters of the model for Figs. 6 and 7.

K (GPa)	μ (GPa)	c_0 (MPa)	p_0 (MPa)	p_1 (MPa)	γ^* (%)	ε^* (%)	h	r	m	n_2
7.6	2.7	1.0	30	120	1.10	25	25	1.2	2.0	2.0

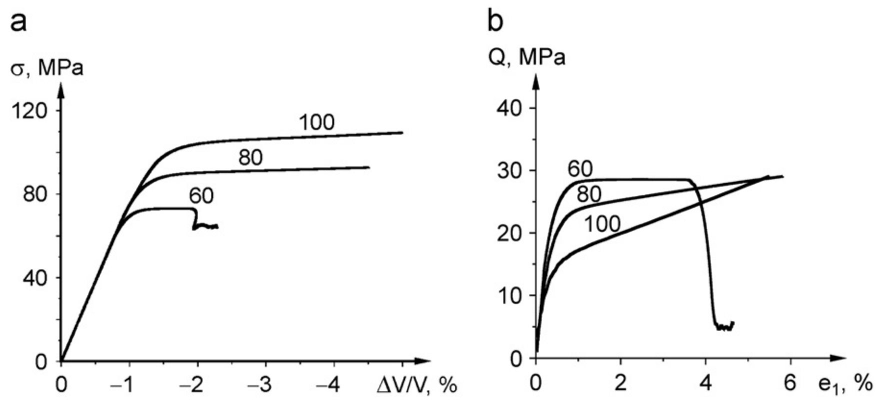

Fig. 7. Plastic deformation of porous sandstone at lateral pressure σ^c=60, 80, 100 MPa. Mean pressure versus volumetric strain of specimen (a) and differential stress $Q=\sigma^1-\sigma^c$ versus axial strain of specimen (b).

The plateau on the curves in Fig. 6(b) corresponds to the initial most severe stage of compaction when porosity variation is yet too small to cause considerable hardening. As the rock porosity reduces, the curve slope increases and approaches the slope in the elastic stage, which is the result of cap surface expansion described by (7). In theory, under very high hydrostatic compression, when pore space would tend to zero, the bulk modulus of the compacted material should tend to the elastic bulk modulus of solid skeleton, which is higher than the elastic bulk modulus of the initial porous material and the slope of the curves in Fig. 6(b) should, actually, increase beyond the elastic one. However, to simplify the model and reduce the number of its parameters, the elastic moduli are assumed as being unchanged.

To analyze the influence of confining pressure on the compaction, we collected the results of deformation simulations at three different (60, 80, 100 MPa) lateral pressures Figs. 7–9, 11, and 12. The calculated loading curves in Figs. 7–8 agree qualitatively with the experimental ones in Fig. 10, schematically adapted from Fortin et al. (2005, 2006). Large stress drops due to stress relaxation during localization banding often observed in experimental curves (Fig. 10(b)) are sometimes not so clear on calculated curves (Fig. 7(b)), where they have much smaller amplitude.

Calculated loading curves presented in Fig. 7, which were obtained with material properties from Table 1, qualitatively agree with Fig. 1(b) based on experimental evidence. At higher confinement the stress path crosses the cap surface with lower differential stress Q, therefore higher confining pressure results in lower yield strength on stress–strain diagrams in Fig. 7(b) and Fig. 1(b). Higher confining pressures also result in higher hardening rates. Since the stress state stays on the curved cap yield surface expanding in the direction of pressure line, the increase of the differential stress is fastest for the rightmost stress state points. At the same time, deformation patterns in these calculations contain mostly localized shear

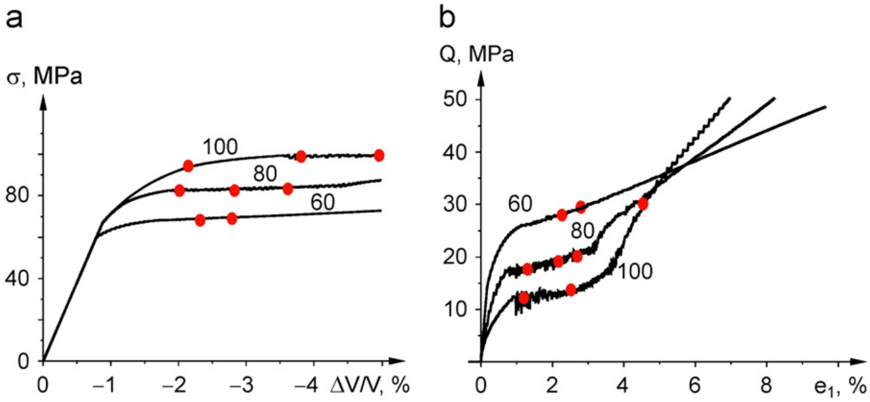

Fig. 8. Numerical simulation results for deformation of porous sandstone at lateral pressures $\sigma^c = 60$, 80, 100 MPa. Mean pressure versus volumetric strain (a) and differential stress $Q = \sigma^1 - \sigma^c$ versus axial strain (b).

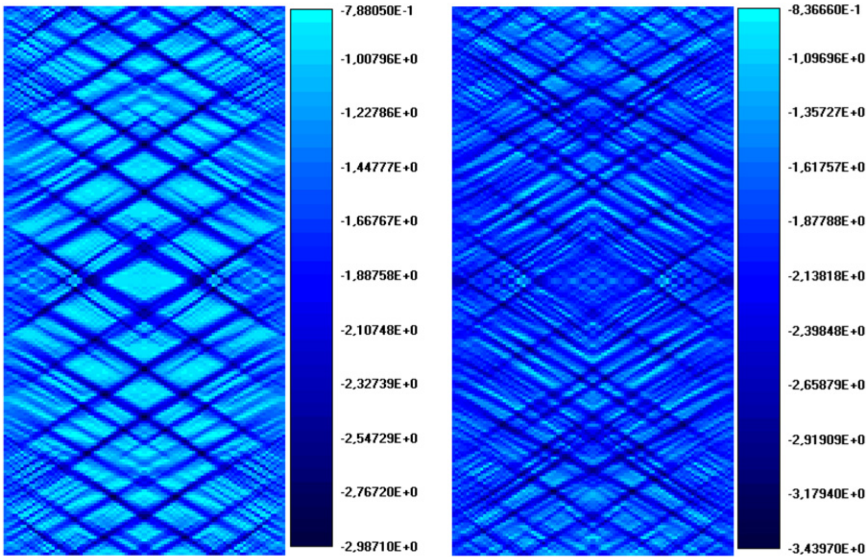

Fig. 9. Shear-compaction bands in axial compression of porous sandstone specimens at $\sigma^c = 60$ MPa. Volumetric strain distribution at successive moments of time.

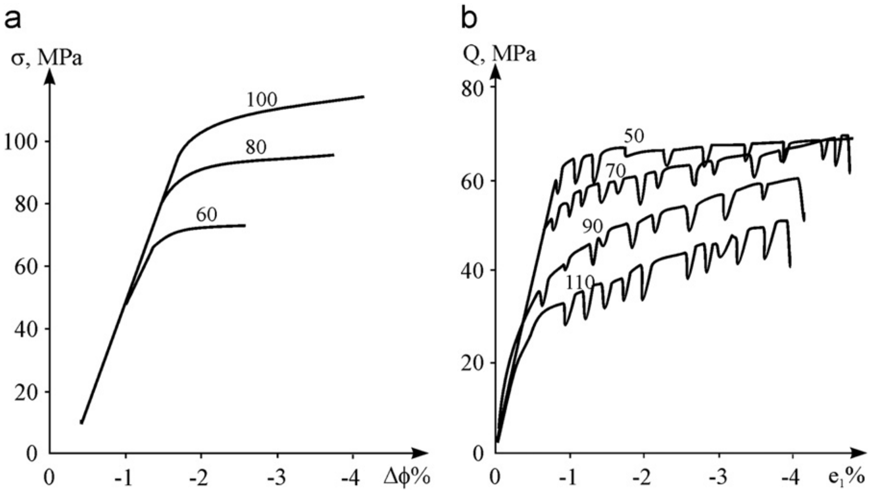

Fig. 10. Mean stress versus volumetric strain (porosity reduction) of tested laboratory samples (a), and differential stress versus axial strain (b) at different confining pressures, adapted from Fortin et al. (2005, 2006).

strain bands with compaction with low level of localization and without noticeable pure compaction bands, which are of main interest for this study. Therefore, in the further series of calculations rock parameters have been changed to promote localization and more compactive behavior (Table 2). Key changes in the parameters are lower hardening h and decreased parameter n_2, which controls variation of dilatancy coefficient with volumetric stress (11). The lower n_2, as follows from (11), should result in more compactive behavior defined by the plastic potential (10) for the same values of mean stress.

Depending on rock properties and loading conditions, the deformation process develops in quite different fashions. For example, calculated deformation patterns exhibited formation of a shear strain localization band with compaction (Figs. 7 and 9) or formation of compaction bands (Figs. 8–9, 11 and 12), and degree of strain localization varied from very high to nearly uniform deformation in the specimen.

Calculated loading curves for the second set of parameters are presented in Fig. 8. As in Fig. 7, larger confining pressure results in larger axial stress and lower differential stress is required to initiate plasticity. Localization of bands illustrated in Figs. 9, 11 and 12 is manifested as oscillations clearly visible on the loading curves. Dots on the loading curves in Fig. 8 correspond to different stages of the deformation process presented in Figs. 9, 11 and 12. At 60 MPa confining pressure, deformation develops in the form of localized shear strain bands with compaction; the number of activated bands increases as the loading progresses. There are two systems of crossing bands inclined at two different angles to the horizontal line. The more inclined bands are activated at the earlier stage of deformation; the bands more aligned with the horizontal line are activated at the later stage. At higher confining pressures (Figs. 11 and 12), deformation develops in the form of nearly horizontal localized compaction bands without noticeable shear strain. As the loading progresses, either compaction bands multiply in numbers or existing bands accumulate more compaction and expand, until the compacted area covers nearly the whole volume of specimen. At moderate confinement in Fig. 11 (80 MPa), multiplication of bands is more pronounced, and at high confinement in Fig. 12 (100 MPa) expansion and smearing of existing bands is more pronounced.

Simulation results presented in Fig. 13 demonstrate the effect of the yield surface expansion rate controlled by parameter m in (7) on the localization degree (confining pressure $\sigma^c = 80$ MPa). The lower values of m result in the slower expansion of the cap surface with the increasing compaction and higher degree of localization. A larger hardening generally results in more uniform distribution of deformation.

Table 3 summarizes the influence of parameters m, n_2 and confining pressures on the final deformation pattern. The parameter denoted as $\Delta\phi_{max}(\%)$ characterizes the degree of localization calculated as the maximum difference of volumetric strain inside and outside the localization bands, and the symbol "$\times$" denotes the formation of shear bands

Table 2
Parameters of the model for Figs. 8–12 and Table 3.

K (GPa)	μ (GPa)	c_0 (MPa)	p_0 (MPa)	p_1 (MPa)	γ^* (%)	ε^* (%)	h	r	m	n_2
7.6	2.7	1.0	30	120	0.8	25	10	1.2	2.0	0.5

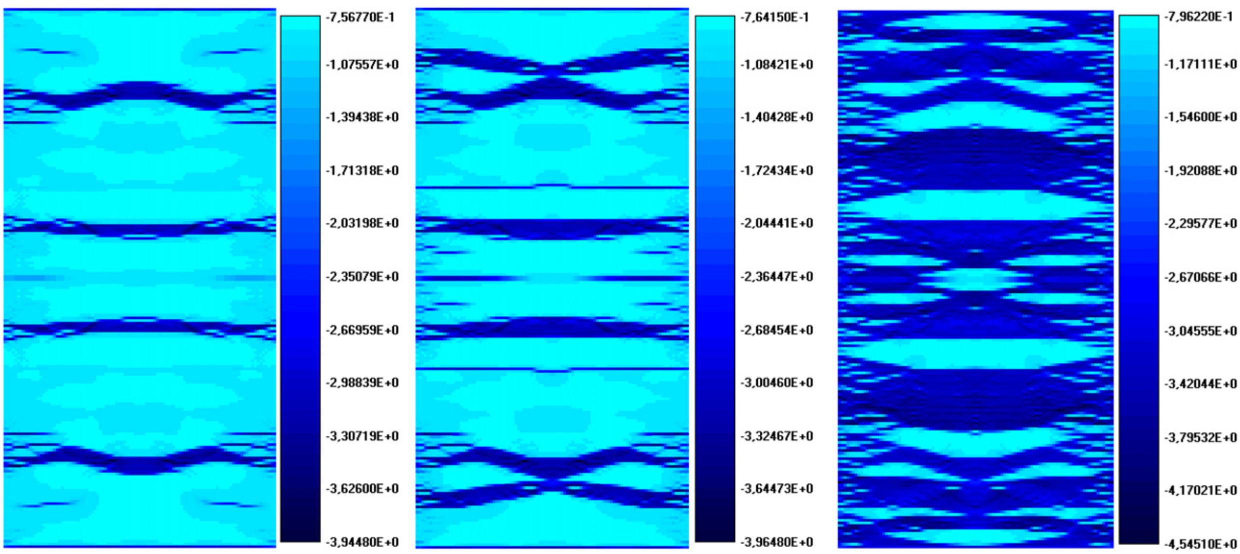

Fig. 11. Formation and smearing of compaction bands in axial compression of porous sandstone specimens at $\sigma^c = 80$ MPa. Volumetric strain distribution at successive moments of time.

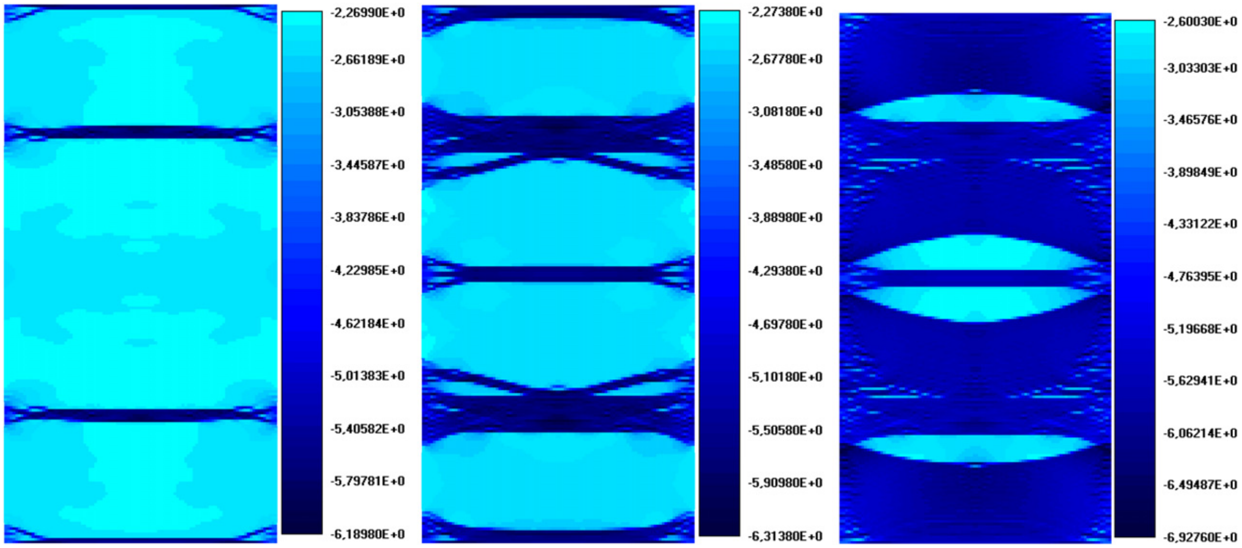

Fig. 12. Formation and smearing of compaction bands in axial compression of porous sandstone specimens at $\sigma^c = 100$ MPa. Volumetric strain distribution at successive moments of time.

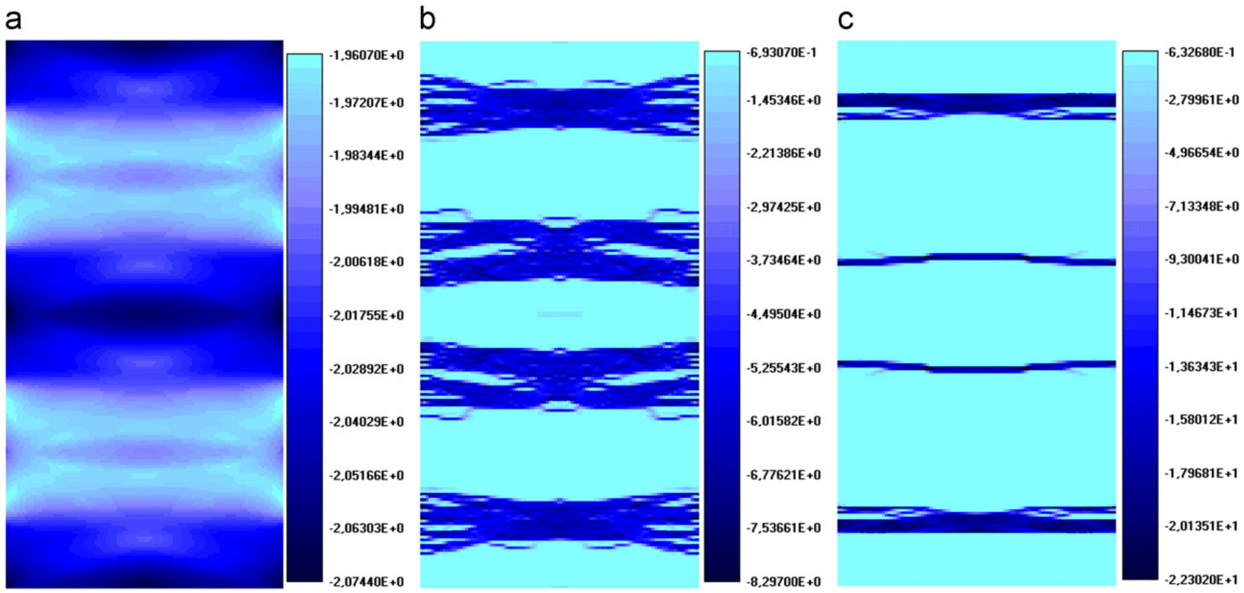

Fig. 13. Compaction bands at different values of parameters of the yield surface expansion: $m=4$ (a), 1 (b) and 0.25 (c). ($\sigma^c = 80$ MPa).

Table 3
Compaction band formation and localization degree for different model parameters.

m	n_2	$\Delta\phi_{max}$ ($\sigma^c=60$)	$\Delta\phi_{max}$ ($\sigma^c=80$)	$\Delta\phi_{max}$ ($\sigma^c=100$)
0.5	0.50	×	15.0	16.0
0.5	1.00	×	×	7.0
1.0	0.50	×	8.0	7.5
1.0	0.75	×	×	3.0
1.5	0.50	×	4.0	4.0
1.5	0.75	–	–	–
2.0	0.50	×	4.1	4.3

with compaction. The symbol "−" denotes that at $m=1.5$ and $n_2=0.75$ there is no noticeable strain localization at confining stresses $\sigma^c=60$, 80, 100 MPa. Table 3 indicates that along with the characteristics of the yield surface, the pressure range, at which compaction bands are formed also depends on plastic potential; that is, on the dilatancy coefficient at a given point of the stress space. For the same values of m, the lower values of n_2 result in formation of localized compaction bands at the lower confining stress.

Note the principal difference between compaction and shear localization in the specimen: shear band formation is typically accompanied by stress relief, as indicated by a descending portion of the loading curve as in Fig. 7 (60 MPa). Compaction band formation does not lead to lasting stress relief. In some cases the strain curve has only a rough plateau and subsequent stress growth, as shown on the 80- and 100-MPa confinement curve in Fig. 8. A drop in stress only appears under conditions when compaction occurs together with an intensive shear or if a shear band with compaction is formed, as in Figs. 9, 14 and 15(c).

Compression of specimens at confining stresses from 60 to 100 MPa considered above ensures that the loading path reaches the yield surface at the rightmost part of the cap surface, where the mean stress is much higher than the shear stress. The next series of simulations are aimed at the analysis of the onset and development of plasticity in the intermediate pressure range, when the initial cap surface is crossed close to the topmost part of the failure envelope in

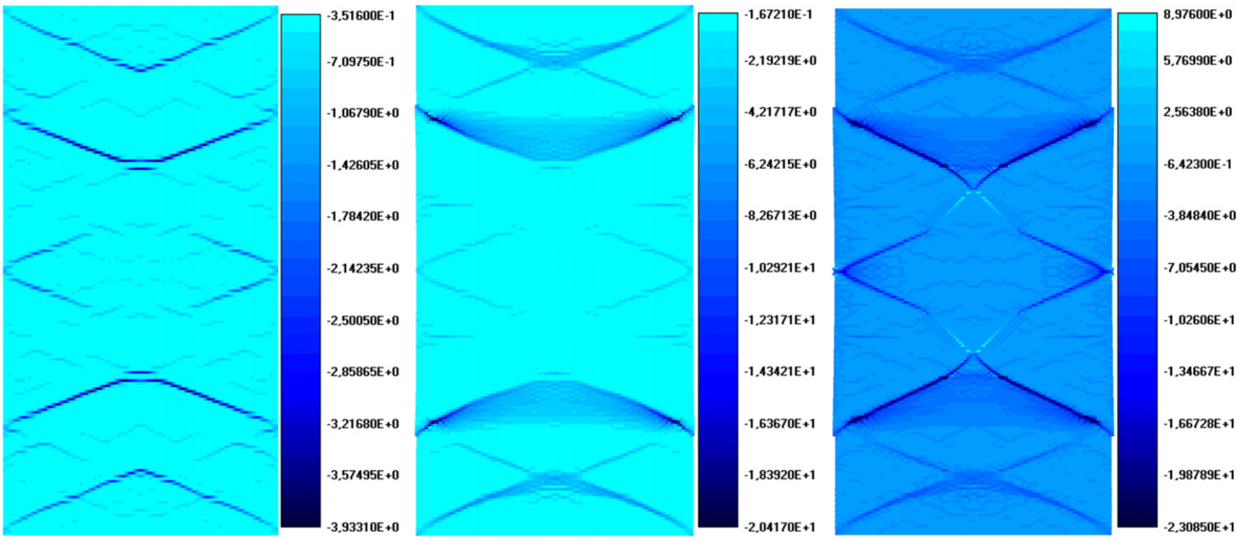

Fig. 14. Compaction bands in axial compression of porous sandstone specimens at lateral pressure 25 MPa. Volumetric strain distribution (%) at successive moments of time.

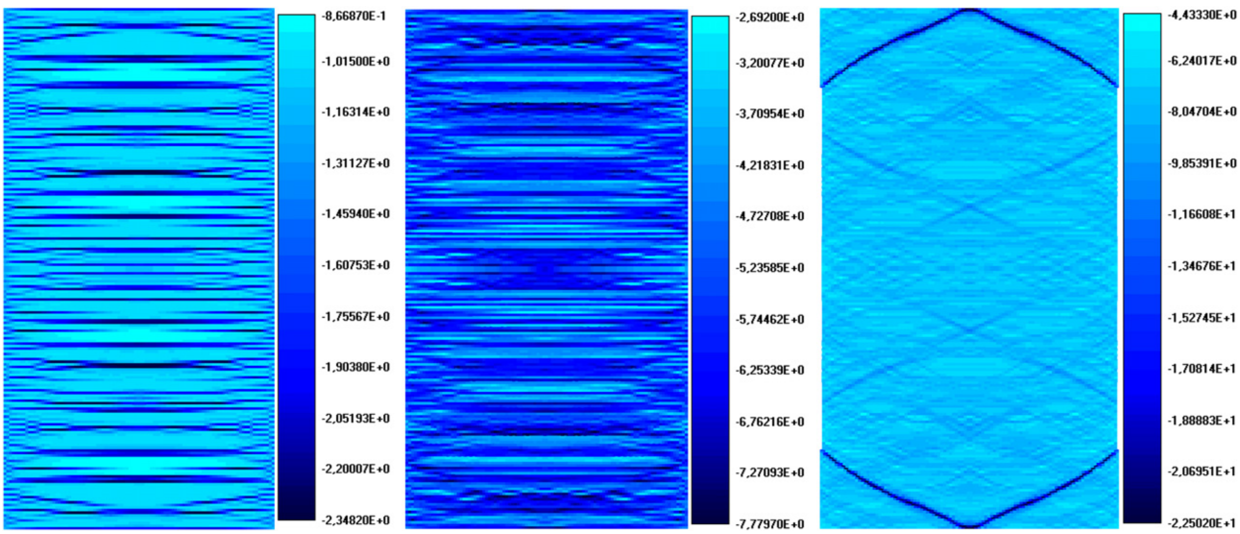

Fig. 15. Compaction bands in axial compression of porous sandstone specimens at lateral pressure 50 MPa. Volumetric strain distribution (%) at successive moments of time.

Fig. 2, when the σ is only a little above the σ_0. These simulations in Figs. 14 and 15 have been performed with slightly modified rock properties (Table 4) to enhance compaction localization further.

At lower confining pressure (25 MPa), Fig. 14, deformation is developed in the form of shear bands with compaction. Further, during deformation, these bands are smeared and compaction becomes more uniform in the specimen. The inhomogeneous stress state, especially at higher stresses, governs the possible development of dilatancy in some zones, i.e., medium loosening. Such zones where volumetric deformation is positive can be observed in Fig. 14(c). This observation suggests that under certain conditions the different plasticity mechanisms such as shear with compaction and shear with dilatancy can be easily mixed inside a single specimen, and local dilatancy can come into play later than compaction.

At higher confinements (50 MPa, Fig. 15), the compaction starts in the form of multiple, thin, horizontal compaction bands. The number of compaction bands in Fig. 15 is higher than in the deformation patterns under higher confinement in Figs. 11 and 12, thanks to introduced changes of parameters. When further deformation occurs with stress growth, it can be accompanied by both the expansion of these horizontal compaction bands and by the formation of new ones until the conditions for formation of inclined shear bands accompanied with further compaction appear (Fig. 15(c)). The switching from compaction via horizontal bands to compaction via inclined shear with compaction bands takes place when all the porosity available for pure compaction is exhausted; cap expansion controlled by (7) moves the stress path closer to the topmost point of the failure envelope, and the dilatancy coefficient in (11) is shifted towards more shear.

A very interesting outcome observed in the simulations is that under heterogeneous conditions governed by the rock fabric or peculiarities of load application the loading path can be different for two neighboring points while equilibrium between the points is retained. For example, in compaction the loading paths of the two points can diverge, when one of them moves up the yield surface – τ increases with decreasing σ – while the other can move in the direction of pressure growth and lower τ (Fig. 16). In this case the specimen equilibrium is retained while the strain increase in different points is different. The process is illustrated in Figs. 17 and 18, which show the loading paths of the two neighboring points of specimens given in Figs. 14 and 19, respectively. One of the points lies in the localization band while the other is outside. Up to a certain moment, the loading paths of these specimen points coincide. After a certain moment, their loadings are developed by different paths, and consequently deformation develops differently.

Table 4
Parameters of the model for Figs. 14–16.

K (GPa)	μ (GPa)	c_0 (MPa)	p_0 (MPa)	p_1 (MPa)	γ^* (%)	ε^* (%)	h	r	m	n_2
7.6	2.7	7.0	50	100	1.0	30	6	1.5	0.75	2

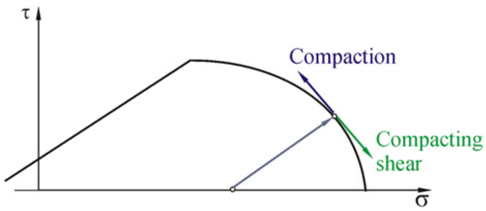

Fig. 16. Scheme of stress path change in localization zone.

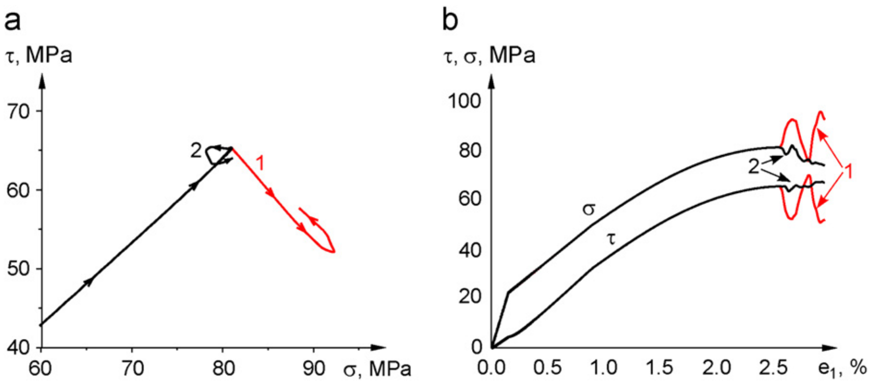

Fig. 17. Loading paths (a) and stress state versus axial strain of the specimen (b) for two different points inside the specimen. Point 1 lies within the shear-compaction band, point 2 is chosen outside localization areas (loading and deformation pattern as per Fig. 14).

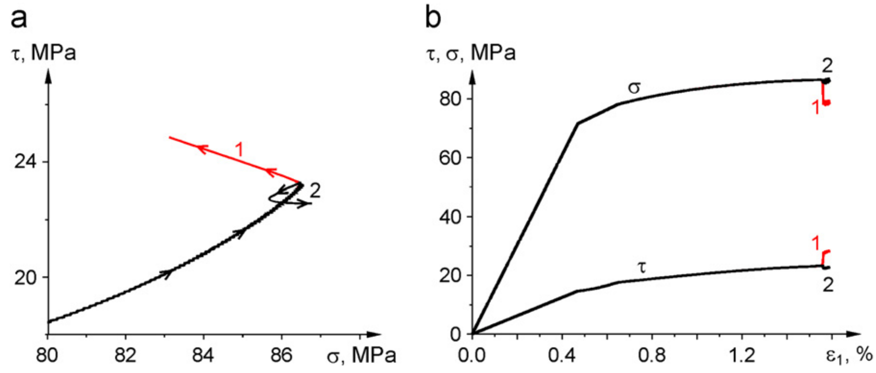

Fig. 18. Loading paths (a) and stress state versus axial strain (b) for two different points: inside(1) and outside(2) of the compaction band. The deformation pattern is shown in Fig. 19.

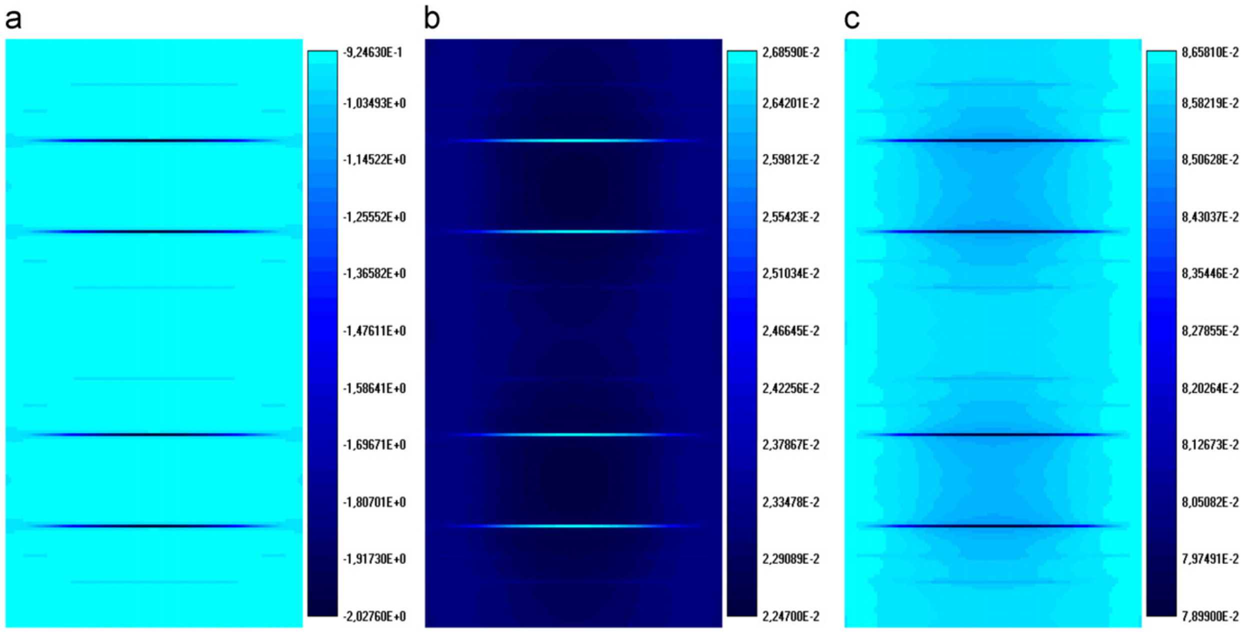

Fig. 19. Volumetric strain distribution, % (a), shear stress intensity τ, MPa (b) and mean stress σ, MPa (c) in the beginning of compaction band formation, $\sigma^c = 80$ MPa.

Note the opposite character of changes in the loading paths in Figs. 17 and 18. Fig. 17 corresponds to the shear-compaction band formation (material properties are represented in Table 4). The stress state of a point positioned in the shear-compaction localization zone changes in the direction of pressure increase with a corresponding decrease in the shear stress intensity. The loading path for the compaction band formation (Fig. 18) shifts towards a pressure reduction and shear stress increase (material properties are represented in Table 5). This is evident in Fig. 19, which shows distributions of volumetric strain, pressure and shear stress intensity. Inside the localized compaction bands, the pressure value is lower while the shear stress intensity value is higher than in the surrounding medium.

In a real rock with a heterogeneous structure, the stress state is always inhomogeneous. Therefore it always has prerequisites for deformation development with different loading paths at different points. Development of localization patterns in initially homogeneous simulated samples may seem confusing. However, a dynamic approach used in the current means that there are always some small disturbances of the stress state caused by the elastic wave propagation even in ideal body made of a homogeneous material. With these disturbances the body is not an ideal homogeneous one anymore. This feature of the dynamic method allows us to easily simulate deformation processes accompanied by localization of plastic deformation and fracturing without introducing additional heterogeneities as seeds of instability into the rock properties. Although the initial minute seed of heterogeneity is considered random, the further development of the localization zone is governed by the conditions of external loading and properties of the rock. For example, if the stress state is close to failure on the cap (Fig. 2), the appearance of point-like seed of negative volumetric strain results in the stress concentration and possible further failing in the regions directed alongside of the minimum stress direction.

Table 5
Parameters of the model for Figs. 18 and 19.

K (GPa)	μ (GPa)	c_0 (MPa)	p_0 (MPa)	p_1 (MPa)	γ^* (%)	ε^* (%)	h	r	m	n_2
7.6	2.7	1.0	40	110	1.0	30	10	2.0	1.5	0.5

It means that the configuration of external loading is the main driver of the localization pattern. It can be also noted, that usage of a dynamic method with good time resolution is important for the successful simulation of highly non-linear process of strain localization. Usage of an implicit iterative quasistatic stress solver with too large stepwise loading increments may over-smooth the stress fields and prohibit strain localization.

Thus, analyzing and determining conditions for localization of compaction require attention primarily paid to a stress path that is governed by loading conditions. The local loading is defined not only by instantaneous parameters of the yield surface and plastic potential, but their variation as functions of the local stress–strain state. Different loading conditions and loading paths in different points of a deformable body are major difficulties for the prediction of compaction band formation. The same is relevant for shear localization.

6. Conclusion

Available experimental evidence of compaction and results of numerical simulations suggest that describing the compaction process of porous rocks critically requires taking into account the yield surface evolution during deformation. Therefore, the emphasis in this work has been on the formulation of functions describing the yield surface variation during deformation, which allow comprehensive modeling of localized compaction and shear while keeping the number of model parameters reasonably small, and on the analysis of the process of development and localization of inelastic deformation in porous rocks by means of computer experiments. At low pressures, when rock deformation is not accompanied by compaction, we propose to use functions similar to those employed in the model for low porosity rocks but with the more pronounced dependence of dilatancy coefficient on mean pressure. At pressures exceeding the threshold value of the compaction onset, model parameters are functions of porosity or volumetric deformation and shear strain. Significantly, this approach also simulates damage accumulation during shear deformation. The dependence of the yield surface expansion on porosity variation (or volumetric deformation) is proposed. Our combined model represents behavior of porous rocks for a wide range of loads as it unites the main advantages of the modified Drucker–Prager–Nikolaevskii and Grueschow and Rudnicki models.

The proposed model has been used to analyze the compaction process of porous sandstone. We have demonstrated the influence of constitutive parameters and functions for the yield surface variation on the deformation pattern and compaction band formation and analyzed it by several test cases. Loading curves and formation of localization bands illustrate the effects of various values of confining pressure acting on the specimens.

This analysis of deformation processes of sandstone specimens has shown that different mechanisms of inelastic deformation can be manifested simultaneously. At compaction band formation, dilation bands can appear in some regions of the specimen. Therefore, for a complete description of the behavior of porous rocks under loading all phenomena should be taken into account: dilation, compaction, and interaction between them. Simple parametric analysis of constitutive relationships with prescribed evolution of stress state is not sufficient to capture all this effects, because it assumes homogeneous stress state. Direct numerical experiment, which is controlled only by prescribed boundary conditions and selected material model, would allow self-consistent description of heterogeneous stress–strain state, because development of heterogeneity is defined by stress–strain evolution itself.

Most pronounced localization band formation is observed when porosity is maximal and cap expansion rate is minimal, which usually corresponds to early stages of compaction. Cap expansion and hardening is manifested by increasing number of compaction bands and increasing width of bands. During localization band formation, both in computer experiment and in real rock, neighboring points can be loaded by different paths, which can be governed by three factors: heterogeneous rock structure, inhomogeneous stress–strain state, and dynamic disturbance of the stress state. As localization starts, loading paths of points lying in and outside the localization band their direction abruptly. Calculations allow us to represent the difference in the stress state variation in localization zones during shear and compaction band formation. The stress path of the point lying in the localization shear-compaction zone changes its direction towards pressure increase with the corresponding decrease in the shear stress intensity. The stress path for compaction band formation turns towards pressure reduction and shear stress growth. In compaction bands, the pressure value is lower while the shear stress intensity value is higher than in the surrounding medium. The existence of different stress paths at nearby medium points and increasing heterogeneity of stress state inside and near the compaction bands can complicate the analysis and interpretation of experiments.

Our algorithm could be most useful for solving scientific problems helping to understand and interpret mechanisms of strain evolution under various conditions and for verification of estimations of the stress–strain state and its presumed evolution obtained by other, simpler methods. The biggest advantage of the suggested method is its ability to account for formation and development of strain localization zones, which are of special interest for geomechanical processes.

Acknowledgments

The authors are grateful to Schlumberger for permission to publish this work. Many thanks to M. Thiercelin for initiating this research; to E. Siebrits for support; to R. Suarez-Rivera and two anonymous reviewers for useful remarks that helped to improve the paper.

References

Baud, P., Vajdova, V., Wong, T., 2006. Shear-enhanced compaction and strain localization: inelastic deformation and constitutive modeling of four porous sandstones. J. Geophys Res. 111 (B12), B12401, doi:10.1029/2005JB004101.
Cuss, R.J., Rutter, E.H., Holloway, R.F., 2003. The application of critical state soil mechanics to the mechanical behavior of porous sandstones. Int. J. Rock Mech. Mining Sci. 40 (6), 847.
de Borst, R., Groen, A.E., 2000. In: Zaman, M., Gioda, G., Booker, J. (Eds.), Computational Strategies for Standard Soil Plasticity Models. John Wiley & Sons, New York, pp. 23.
Drucker, D.C., Prager, W., 1952. Soil Mechanics and plastic analysis or limit design. Q. Applied Math. 10 (2), 157–165.
DiMaggio, F.L., Sandler, I.S., 1971. Material models for granular soils. J. Eng. Mech. ASCE 97, 935–950.
El Bied, A., Sulem, J., Martineau, F., 2002. Microstructure of shear zones in Fontainebleau sandstone. Int. J. Rock Mech. Mining Sci. 39, 917–932.
Fortin, J., Schubnel, A., Guéguen, Y., 2005. Elastic wave velocities and permeability evolution during compaction of Bleurswiller sandstone. Int. J. Rock Mech. Mining Sci. 42, 873–899.
Fortin, J., Stanchits, S., Dresen, G., Guéguen, Y., 2006. Acoustic emission and velocities associated with the formation of compaction bands in sandstone. J. Geophys. Res. 111, B10203, doi:10.1029/2005JB003854.
Fossen, H., Schultz, R.A., Shipton, Z.K., Mair, K., 2007. Deformation bands in sandstone: a review. J. Geol. Soc. London 164, 755–769.
Garagash, I.A., 2006. Conditions of the formation of regular systems of shear and compaction bands. Russ. Geol. Geophys. 47, 655–666.
Garagash, I.A., Nikolaevskii, V.N., 1989. Nonassociated flow rules and localization of plastic deformation. Usp. Mekh. 12 (1), 131–183 in Russian.
Grueschow, E., Rudnicki, J.W., 2005. Elliptic yield cap constitutive modeling for high porosity sandstone. Int. J. Solids Struct. 42, 4574–4587.
Issen, K.A., Challa, V., 2003. Conditions for dilation band formation in granular materials. In: Paper Presented at the 16th ASCE Engineering Mechanics Conference. 〈http://www.ce.washington.edu/em03/proceedings/papers/638.pdf〉.
Issen, K.A., Challa, V., 2006. Influence of the intermediate principal stress on compaction localization conditions. In: Paper Presented at the 41st US Symposium on Rock Mechanics, American Rock Mechanics Association.
Issen, K.A., Rudnicki, J.W., 2000. Conditions for compaction bands in porous rock. J. Geophys. Res.—Solid Earth 105, 21529–21536.
Karner, S.L., Chester, F.M., Kronenberg, A.K., Chester, J.S., 2003. Subcritical compaction and yielding of granular quartz sand. Tectonophysics 377, 357–381.
Klein, E., Baud, P., Reuschle, T., Wong, T.-F., 2001. Mechanical behaviour and failure mode of Bentheim sandstone under triaxial compression. Phys. Chem. Earth A 26, 21–25.
Nagel, N.B., 2001. Compaction and subsidence issues within the petroleum industry: from Wilmington to Ekofisk and beyond. Phys. Chem. Earth. Part A: Solid Earth Geodesy 26 (1-2), 3–14.
Nikolaevskii, V.N., 1971. Governing equations of plastic deformation of a granular medium, J. Appl. Math. Mekh. 35, 107–1082.
Nikolaevskii, V.N., 1972. Mechanical properties of soils and plasticity theory. In: Solid Mechanics, vol. 6, VINITI AN SSSR, Moscow, p. 5 (in Russian).
Nikolaevskii, V.N., 1996. Geomechanics and Fluidodynamics: With Applications to Reservoir Engineering, Dordrecht–Boston. Kluwer Academic Publishers.
Okubo, C.H., Schultz, R.A., 2005. Evolution of damage zone geometry and intensity in porous sandstone: insight gained from strain energy density. J. Geol. Soc. 162, 939–949.
Olsson, W.A., 1999. Theoretical and experimental investigation of compaction bands in porous rock. J. Geophys. Res. 104, 7219–7228.
Rudnicki, J.W., 2004. Shear and compaction band formation on an elliptic yield cap. J. Geophys. Res. B. 109 (B3), B03402, doi:10.1029/2003JB002633.
Schubnel, A., Fortin, J., Burlini, L., Guéguen, Y., 2005. Damage and recovery of calcite rocks deformed in the cataclastic regime. In: Bruhn, D., Burlini, L. (Eds.), High-Strain Zones: Structure and Physical Properties. Geological Society of London, London, pp. 203.
Schultz, R.A., Siddharthan, R., 2005. A general framework for the occurrence and faulting of deformation bands in porous granular rocks. Tectonophysics No. 411, 1–18.
Schutjens, P.M.T.M., Hanssen, T.H., Hettema, M.H.H., Merour, J., de Bree, P., Coremans, J.W.A., Helliesen, G., 2004. Compaction-induced porosity permeability reduction in sandstone reservoirs: data and model for elasticity-dominated deformation. SPE Reservoir Evaluation and Engineering 7 (3), 202–216.
Stefanov, Y.P., 2002. Deformation localization and fracture in geomaterials. Numerical simulation. Phys. Mesomech. 5 (5-6), 67.
Stefanov, Y.P., 2004. Numerical investigation of deformation localization and crack formation in elastic brittle-plastic materials. Int. J. Fract. 128 (1), 345–352.
Stefanov, Y.P., 2005. On some features of numerical simulation of the behavior of elastic-brittle-plastic materials. Phys. Mesomech. 8 (3–4), 121–133.
Stefanov, Y.P., Thiercelin, M., 2007. Modeling of the behavior of highly porous geomaterials at compaction band formation. Fiz. Mezomekh. 10 (1), 93–106 in Russian.
Swan, C.C., Seo, Y-K., 1999. Limit state analysis of earthen slopes using dual continuum/FEM approaches. Int. J. Numer. Anal. Meth. Geomech. 23, 1359–1371.
Tembe, S., Baud, P, Wong, T.-f, 2008. Stress conditions for the propagation of discrete compaction bands in porous sandstone. J. Geophys. Res. 113, B09409 , doi:10.1029/2007JB005439.
Wilkins, M.L., 1964. Calculation of elastic–plastic flow. In: Alder, B., Fernbach, S., Rotenberg, M. (Eds.), Methods in Computational Physics. Academic Press, New York, pp. 3.
Wilkins, M.L., 1999. Computer Simulation of Dynamic Phenomena. Springer-Verlag, Berlin–Heidelberg–New York.
Zhu, W., Wong, T., 1997. The transition from brittle faulting to cataclastic flow. Permeability evolution. J. Geophys. Res. B 102 (B2), 3027–3041.